Metals and Materials International (2020) 26:695–707
https://doi.org/10.1007/s12540-019-00368-2

Experimental Analysis of the Aluminium Melting Process in Industrial Cold Crucible Furnaces

Michal Palacz[1] · Bartlomiej Melka[1] · Bartosz Wecki[2] · Grzegorz Siwiec[2] · Roman Przylucki[3] · Piotr Bulinski[1] · Slawomir Golak[3] · Leszek Blacha[2] · Jacek Smolka[1]

Received: 21 March 2019 / Accepted: 7 July 2019 / Published online: 25 July 2019

Abstract
One of the promising technology that guarantee the high-purity of the processed metal is induction skull melting. The quality of the melting process within such a system strongly depends on the cold crucible design. Hence, the experimental investigation of the cold crucible melting was performed. The experimental investigation was performed for various initial mass of the load. The results of that analysis were used for the assessment of the alloy temperature during the process, free surface shape and the area as well as the liquid metal emissivity. The collected results of the thermal analysis showed that the temperature of molten metal increased within the power input increase. Moreover, results of that analysis showed that the characteristic tooth-shaped jags were created mostly at the centre of the cold crucible segments. In addition, experimental results are suitable for the numerical models validation and further investigation of the cold crucible design.

Keywords Cold crucible furnace · ISM · Induction melting · Cold crucible design · Experimental investigation

1 Introduction

Most of industrial sector desires high-purity metals and alloys. Morita et al. [1] underlined that due to the outstanding properties of high-quality titanium alloys such as the corrosion resistance or the biocompatibility, these alloys are more often used as the material for the medical implants. Moreover, Fadeev et al. [2] also pointed out the importance of the high quality alloy for the gas turbine blades. Moreover, the metals used for these state of the art technologies, such as titanium or aluminium, are highly reactive. In consequence, levitation or semi-levitation melting techniques are desirable to guarantee the required quality of the processed metals or alloys. One of the semi-levitation methods is the application of a cold crucible furnace (CCF). As the authors of [3] stated the CCF melting or smelting is usually conducted in a vacuum or neutral atmosphere, e.g., argon. The study presented in [4] showed that a method of metal processing is also interesting from the economic point of view in case of the relatively expensive titanium alloys. Due to an electromagnetic field, the processed metal is pushed away from the crucible walls. Additionally, the crucible walls and the crucible bottom are water-cooled. The high temperature difference between the molten metal and the crucible bottom results in the formation of so-called skull.

Song et al. [5] suggested that the skull works as a protective layer that prevents the contamination of the processed metal from the crucible. Moreover, Sugilal [6] processed various highly reactive metals inside the cold crucible furnace. The authors of the aforementioned study noted that the skull prevents the liquid metal from superheating. On the other hand, the skull can be considered as a loss of the crucible load. Therefore, the crucible construction should be carefully designed to minimise the skull mass. Moreover, the melting procedures should be adjusted for a selected mass and shape of the load.

The general design of the cold crucible furnace is the same regardless of the applied melting method. The typical construction of CCF is an assembly of the segmented crucible walls and the coil that surrounds the crucible. The crucible segments are separated from each other by thin slits.

✉ Michal Palacz
michal.palacz@polsl.pl

[1] Institute of Thermal Technology, Silesian University of Technology, Konarskiego 22, 44-100 Gliwice, Poland

[2] Institute of Metal Technology, Silesian University of Technology, Krasinskiego 8, 40-019 Katowice, Poland

[3] Departament of Industrial Informatics, Silesian University of Technology, Krasinskiego 8, 40-019 Katowice, Poland

In consequence, the crucible is, to some extent, transparent for the electromagnetic field. Therefore, the crucible operates as a secondary inductor. As previously mentioned, the crucible walls, the bottom and the coil are cooled by the water flowing through the internal ducts of these components. Therefore, the segments of the crucible and its bottom remain significantly colder than the metal or alloy inside the crucible. In the case of the investigated crucible, the cooling channels of the crucible walls were separated from the crucible bottom channel. A more detailed description of the investigated crucible is provided in Sect. 2 of this paper. Despite the relatively simple crucible assembly, the recent studies demonstrated that the crucible performance is strongly related to the crucible design. The relation between the crucible design and its performance was investigated by numerous authors. The authors of [7] reported that the number of the crucible segments, as well as the width of the slits between the segments, affects the electromagnetic field significantly and, in consequence, the crucible performance. Similar analysis was presented in [8]. The authors of that work investigated the crucible wall arrangements on the efficiency of the melting in CCF. In addition, the influence of the number of the walls segments as well as the slits thickness was investigated by these authors. According to the presented results, the design of the crucible walls significantly affects the electrical performance of the device. Dumont et al. [9] showed that depending on the crucible design the efficiency of the crucible can vary from 26% to 53%. The analysis of the cold crucible used for melting and direct solidification of titanium alloys was showed in [10]. The results presented by these authors showed how the crucible performance vary with the change of the coil position, a ratio of the metal height to length or magnetic Reynolds number. The results gathered by [10] showed that the proper crucible design and melting process are beneficial for the crystallization of the alloy during the process. Moreover, the results presented in [10] showed the good agreement with the cold crucible experimental analysis presented in the papers such as [11]. Accounting for the importance of the crucible design and the influence of the melting procedure on the performance of the melting method, the mathematical models of the CCF have recently been employed to investigate the device performance.

The metal melting is a relatively complex phenomenon. Therefore, the numerous authors investigate that process both experimentally and numerically. In particular, the free surface shape, the convection flow and the temperature field of the molten metal are the scope of the various studies. Keneda et al. [12] investigated the natural convection flow under the uniform magnetic field. The authors of that work underlined the relation between the convection, Lorentzen forces and the heat rate under various electric current. It is worth mentioning that Kenda et al. investigated the process both experimentally and numerically. The free surface characteristics of the molten metal were also investigated in [13]. Li et al. [13] conducted the number of tests on the dedicated experimental stand to analyse the free surface structure and convective heat transfer. However, the considered liquid metal flow was laminar in that case.

Taking into account the complexity of the phase change and the multiphase flow during metal melting and the difficulties related to the experimental investigation of that process, the mathematical models are more often used to simulate the flow and the phase change of the metal [14]. In particular, mathematical models that are applied during the CCF analysis should include phenomena such as the phase change of the metal during the melting, free surface fluctuations, heat transfer in the load and the crucible and the mixing of the liquid metal. Therefore, i.e. Spitans et al. [7] proposed the coupling procedure for the electromagnetic and heat and fluid transfer models. In such an approach, each sub-model should be carefully developed and validated to guarantee the satisfying results. The analogical approach for the induction melter and analysed the influence of the turbulence models on the velocity and the free surface shape prediction was used in [15]. The results gathered by the authors of that study showed the significant difference between the velocity fields and vortices obtained by utilisation of the $k-\epsilon$, $k-\omega$ and transition SST model. According to those results, the SST model predicted the highest velocity of the molten metal. The $k-\omega$ model was also used by the authors of [16, 17]. That group of the researchers formulated numerical model for the dynamic simulations of the melting process of titanium and titanium alloys. In particular, the authors of [16] proposed axisymmetric pseudo-spectral mathematical formulation for the prediction of the temperature inside the load. In latter paper [17], the authors numerically investigated the influence of the crucible design parameters on the heat losses melting process in the cold crucible. The numerical model together with the experimental results presented in that paper was used to optimise the melting process in the cold crucible. Both experimental and the numerical results showed that the process should be carefully optimised for various loads. In addition, the authors of [17] underlined the relation between the free surface shape and turbulence on the temperature of the molten load. In particular, the authors of [16, 17] concluded that heat losses related to the evaporation of the aluminium from the free surface were significantly higher comparing to the heat loses caused by the radiation. Nevertheless, Bulinski et al. [15] presented that the effects of the turbulence modelling on the Lorentzen force field were negligible. In the other work of these authors [18] the validation of the developed model for the vacuum induction furnace was presented. In the validation procedure, the free surface shape as well as the temperature field were compared. According to the reported results, the acceptable

agreement between the experimental and numerical results was achieved. Recently, Bulinski et al. [19] employed the coupled CFD-EMAG model for the cold crucible furnace. That study was mostly devoted to an identification of the free surface shape and free surface area. Moreover, he compared the obtained numerical results with the experimental data showing a good agreement in terms of the temperature and the free surface shape prediction. Above that, the authors of [20] performed further investigation of the process. In particular, the previously developed numerical model was used for the investigation of the evaporation process in vacuum induction furnace. The mathematical model results were compared with the experimental results in terms of mass evaporation prediction. Next, Bulinski et al. [20] used that CFD-EMAG model to analyse the evaporation process for various crucibles position and metal charges. Considering that the CCF technology is already present in commercial installations, the data used for the validation should be collected during the operation of industrial-type cold crucible furnaces. Unfortunately, the literature dealing with the mathematical modelling of the melting process in the mentioned industrial-type CCFs is fairly limited.

Song et al. [21] experimentally investigated the impurities evaporation from aluminium alloys. The results presented in that paper primarily included the evaporation kinetics, while neglecting the temperature measurements. In addition, Matsuzawa et al. [22] collected pictures of the deformation of the processed aluminium at different times. Next, these pictures were compared with the simulation results. The authors of that study pointed out the number of difficulties that were encountered during that comparison. In consequence, the experimental results presented by these authors are unsuitable for the further validation of the numerical model, especially in case of the industrial-scale CCF systems. Moreover, authors of [22] did not focus on the validation of the thermal analysis that they performed. More detailed analysis of the process was presented in [23]. These authors presented various numerical results for a direct solidification cold crucible system. In that paper, the magnetic flux density and the temperature at the alloy centre were used for the model validation. The comparison of the experimental and numerical results presented by Chen et al. [23] indicated good model fidelity in terms of the temperature and magnetic flux density prediction. However, the presented results were gathered during the investigation of laboratory-scale equipment. Hence, it is difficult to use those results to analyse industrial-scale VIM applications.

Accounting for the lack of experimental results from the industrial CCF systems, which can be used for the mathematical model validation, the scope of this study was to perform the experimental analysis of industrial-scale cold crucible furnace. We focus on the temperature and shape measurements of an alloy composed of 99% aluminium and 1% (mass) zinc that was melted in the considered CCF. The temperature was measured inside the molten metal with an immersion thermocouple, while the temperature of the free surface of the load was measured with an infrared camera. In addition, the emissivity of the liquid metal and the crucible walls was assessed. For the meniscus shape measurements, the in-house device was developed. The shape of the meniscus tip was assessed using that device, while the meniscus bottom and the skull generation phenomena was photographed. To achieve steady-state conditions during the measurements, a melting procedure was developed for various power inputs. All the experiments were performed on the industrial-scale cold crucible furnace that was delivered by the *Seco-Warwick* company. As expected, the results of the temperature assessment demonstrated that the power input increase resulted in the temperature of the free surface increasing. However, the temperature increase was considered to be insignificant. The difference in the free surface temperature for 50% and 65% generator power was of 13%. In consequence , the emissivity of the free surface was considered to be constant for the various power inputs and was of approximately 0.03. The meniscus shape and the free surface area analysis revealed that the melting process was more effective in the case of the 1.6 kg load and the generator power input of 35%. For that set up, the free surface area and the skull mass were similar to those recorded for the 1.3 kg load and 65% of the power input. Finally, during the meniscus analysis, the skull generation process was studied. In consequence, the typical tooth-shaped jags on the skull circumference were noticed. These characteristic jags were identified as being generated at the centre of the crucible wall segments. To the best of our knowledge, such an investigation has not been previously presented in the literature.

2 Cold Crucible Furnace Design

As mentioned in Sect. 1, all experimental tasks were performed on a cold crucible furnace delivered by *Seco-Warwick* in collaboration with the *Retech* company. The general view of the furnace is presented in Fig. 1. That device is supplied by a *Seco-Warwick* generator that offers 200 kW of input power. The furnace control system integrated with the furnace offers measurements of the active power and the actual frequency. Nevertheless, the indication of the built-in control system strongly depends on the accuracy of the inverter resonant system matching. Therefore, the actual current and the frequency were measured at the inductors resonance circuit inside the inverter cabinet. The measured current and frequency are listed in Table 1. The measured values were used to define an approximation function that assessed the current and frequency for any generator load. The approximation functions for the current [Eq. (1)] and

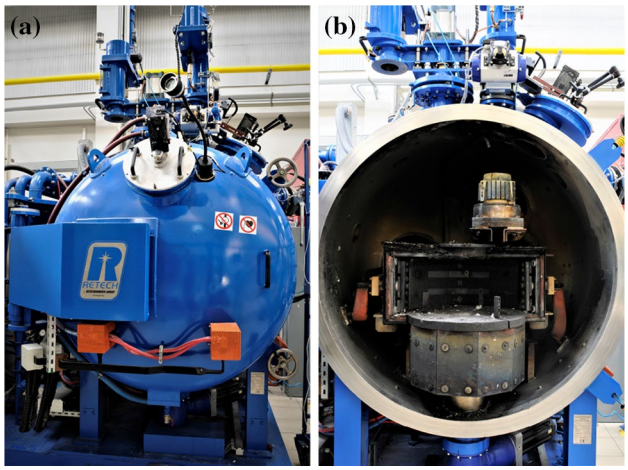

Fig. 1 Overview of the investigated furnace **a** outside and **b** inside

Table 1 Measured values of the current and frequency for various generator loads for aluminium charge

Generator load (%)	Current amplitude, kA	Frequency (kHz)
20	2.44	8.92
40	3.40	7.60
60	4.00	7.35
80	4.60	7.14
100	5.20	7.07

the frequency [Eq. (2)] are presented below. The R^2 for both functions was higher than 0.99.

$$y_I = 1.5520 + 0.049 \cdot x - 0.0001 \cdot x^2 \quad (1)$$

$$y_f = 11.436 - 0.1667x + 0.0022x^2 - 9.68 \times 10^{-6}x^3 \quad (2)$$

To guarantee a vacuum, the investigated furnace is equipped with a set of pumps. The pump system includes a *Kaesser* compressors WVC 1200 rotary vacuum pump (4 kW and 3000 RPM @50 Hz), a *Busch* R5 0100 F rotary vacuum pump (2.7 kW and 1500 RPM @50 Hz) and an *Agilent Technologies* diffusion pump (4.4 kW). Various valves and types of insulations were installed in the furnace to prevent any intake of the surrounding air. The furnace walls, the crucible segments, the bottom and the generator are cooled by water. The water is cooled within a *Parker Hyperchill PWC* industrial chiller, which has a cooling capacity that is rated for 183 kW. The temperature of the water is monitored at the chiller outlet and the crucible outlet. The mass flow rate of the cooling water is not controlled or monitored during the melting process. By default, the temperature of the processed medium is measured by a pyrometer installed directly above the crucible or by an immersion thermocouple that can be sank into the molten metal. However, that set up was adjusted for the titanium melting process. The lowest temperature limit for the pyrometer is slightly lower than the titanium melting temperature and significantly higher than the aluminium melting temperature. Therefore, those device readings were not considered during the study. Fortunately, the immersion thermocouple installed in the furnace can be sank inside the molten metal any time during the process without interfering with the vacuum. Alternatively, the thermocouple can be replaced with a sample collector, which is typically used for the extraction of the liquid metal samples for further chemical analysis. Additionally, the sample collector can be used for the attachment of various measuring devices that can be sank into the metal during the process.

Two inspection windows are installed on the furnace walls. These windows are equipped with industrial cameras. Hence, the melting process can be visually controlled by the operator. Inside the inspection windows, eight additional glasses are installed on a revolver-type frame to prevent the outer window from being damaged. By positioning the revolver-type frame, the glasses can be changed during the melting process. The outer glass is made of calcium fluoride (CaF_2), which is approx. 95% transmissive for the wavelength in the range of 0.13–9.00 µm depending on the glass thickness. Inside the mentioned revolver-type frame, additional CaF_2 glass and germanium glass were installed. The germanium glass guarantees approximately 100% transmission of wavelengths from 8.00 to 12.00 8.00 to 12.00 µm [24, 25]. This configuration is suitable for the middle range infrared (IR) cameras.

2.1 Crucible Design

The crucible installed in the furnace was composed of 16 copper segments. The interior of each segment, as well as the crucible bottom, are water cooled. Hence, the wall temperature of the crucible is significantly lower than the processed medium. The crucible segments are separated by 1 mm slits. Bulinski et al. [19] used a similar crucible design for the numerical investigation of the process. The described crucible is placed inside the inductor coil, which is also cooled by water. The magnetic shunts are adjacent to the coil in order to intensify the magnetic field inside the crucible. The schema of the investigated crucible, as well as the coil design, is presented in Fig. 2. As shown in Fig. 2, the water channels of the bottom and the crucible walls are separated.

The analysed crucible was specifically designed for titanium melting. The maximum mass of titanium that can be melted in that configuration of the inductor and crucible is 2 kg. Notably, the crucible walls are significantly higher than the induction coil. Consequently, melting the load above the

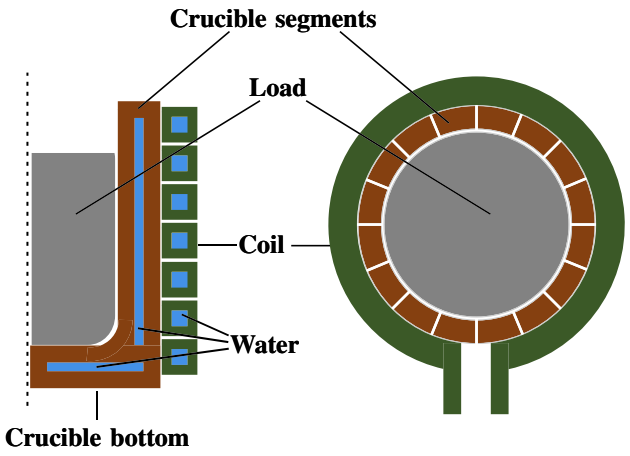

Fig. 2 Schema of the cold crucible furnace

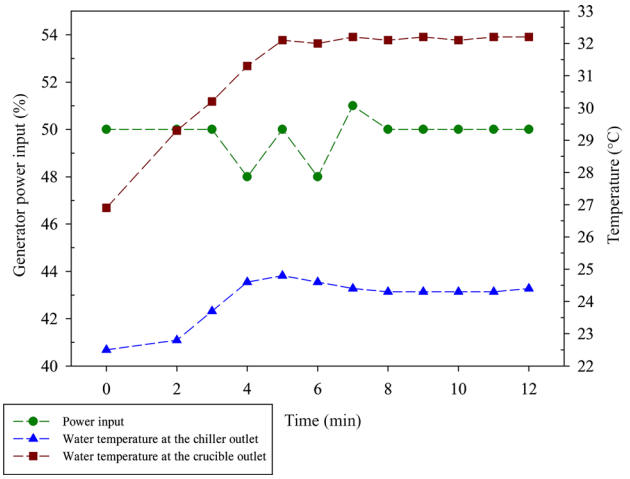

Fig. 3 Time trends of the generator power input (green), crucible outlet water temperature (red) and chiller outlet temperature (blue). (Color figure online)

induction coil is difficult in the case of a high-density metal, e.g., copper. However, lighter metals tend to slip out of the crucible if the amount of material or the power input is too high. Therefore, the correct amount of the investigated metal and a suitable power load must be provided to guarantee the safety and stability of the melting process. That procedure should be carefully modified for the considered variation of the load type and power input.

2.2 Melting Procedure

All the results presented in the paper were collected for aluminium with a zinc addition (1% mass). For such an alloy, the melting procedures were developed to achieve a stable melting process. For each run, the cylinder-shaped load of the aluminium and zinc alloy was prepared. The diameter of the cylinder for all considered cases was 80 mm, while their height varied from 100 to 120 mm. Before the melting process was started the load was weighed. Hence, the initial mass of the metal was known. The diameter of the cylinder-shaped load was slightly smaller than the crucible's inner diameter. Consequently, the initial tilting of the load was avoided.

To achieve the steady/quasi-steady conditions for each melting process the system parameters, such as the power input, the cooling water chiller output, the crucible output temperatures and the vacuum pressure , were monitored during the process. Finally, a special melting procedure was developed to guarantee steady conditions for the analysed load and power input. Before the melting of the metal began, all the inert gases were removed from the furnace using the system of pumps. When the vacuum pressure was 0.2×10^{-2} bar, the metal began to melt. The metal was melted by providing 50% of the generator power. That value corresponds to a 3.8 kA current at a 7.4 kHz frequency. That set up is called Variant A throughout this paper. Variant A offered a stable melting process with all the characteristic stages of meniscus formation. Then, the power input was maintained until the quasi-steady conditions were reached. To control the stability of the process, the power input, the chiller outlet and the crucible outlet water temperatures were monitored. The trends of the monitored values are presented in Fig. 3. The average melting time for the mentioned set up was 5 min. However, as can be seen in Fig. 3, steady conditions were obtained after approximately 9 min. Then, the immersion thermocouple was sunk into the liquid metal for 5 more minutes to measure the temperature of the alloy. That temperature measurements were used for the calibration of the metal emissivity during the IR camera measurements. Moreover, as it is presented in Fig. 3, the power input was steady within the analysed process. The small variation of the power input between the 4th and 6th minutes of the process was caused by the phase change of the alloy. Consequently, the electromagnetic properties of the load changed.

Next, the power input was increased up to 65% of the generator power, which corresponds to a 4.31 kA current at a 7.2 kHz frequency; this set up is called Variant B. The increase in the current resulted in a higher power input and, consequently, influenced the shape and the height of the meniscus. Moreover, the weight of skull gathered at the crucible bottom decreases. Analogous to the melting process with a higher current, after a few minutes, the steady state was recorded. Then, after the measurement recording, the casting of the metal occurred. Next, the power input was switched off, and the furnace was cooled for approximately 30 min. Finally, after cooling the crucible and the cast, the air inlet valves were opened to level the pressure inside the furnace with the ambient pressure. After opening the

furnace, the skull was collected, and the crucible was prepared for another experimental run.

3 Measurement Instruments

As was briefly mentioned in the introduction, the conducted experimental campaign was focused on the molten metal temperature, the meniscus shape measurements and the skull shape. For the temperature field measurements, an advanced IR camera was used, namely, a Flir A655sc, which is equipped with an uncooled microbolometer that operates in the spectral range from 7.5 to 14.0 µm. The maximum frame rate available with the full window (640 × 480 pix) recording is 50 Hz. The 41.3 mm Flir lens, which offers a field of view (FOV) of 15° × 11.3°, was mounted on the camera. The camera together with the lens was calibrated for the temperature range of −40°C to 150°C and the alternative range of 300°C to 2000°C. The accuracy of that camera, as declared by the manufacturer, was rated as ± 2 °C or ± 2% of the reading. The camera was installed on the furnace wall above the inspection window equipped with the glass suitable for the applied camera. The IR camera temperature reading was verified by the immersion thermocouple. Therefore, the emissivity of the molten metal was assessed.

The meniscus shape of the molten metal was measured by a simple but robust in-house constructed tool. The general assessment of the meniscus shape and the measurement of the maximum height was possible with the developed device. The idea of the device was to fix relatively thin wires to the wooden plate. Then, the device was mounted directly above the crucible. Next, the position of the device was set, namely, the tips of the wires touched the top of the solid load. Therefore, when the molten metal meniscus occurred, the molten metal partially stuck to the installed wires. The device scheme is presented in Fig. 4. When the melting and casting processes were performed, the device presented in Fig. 4 was removed from the furnace. Next, the distance between the needles covered with the aluminium alloy and the device base was assessed. Therefore, the approximation of the meniscus shape and maximum height was performed. Moreover, the results gathered using this method are useful for the calculation of the free surface area of a molten medium.

After each experimental run, the generated skulls were collected and weighed to evaluate the loss of molten medium. The shape of the skull was also assessed. The collected material was cut along the diameter to examine the shape and height of the skull near the crucible walls, since the skull shape is especially important from the electromagnetic forces point of view. At the crucible bottom, the generated skull was near the slits between the crucible wall segments. Consequently, the Lorentz force, as well as the velocity field of the liquid alloy, change. The maximum height of the skull is the point where the meniscus adhered to the crucible walls, and thus, that information is useful for assessing the meniscus shape. To better illustrate the relation between the meniscus and the skull, Fig. 5 is presented. The shape of the meniscus tip marked in that figure was measured with the device presented in Fig. 4. The mentioned device was positioned, each time, to collect the points that were then used to reconstruct the shape of the tip. As shown in Fig. 5, the point where the meniscus slope is attached to the crucible walls corresponds to the maximal skull height. Therefore, for a known meniscus tip shape and skull height at the crucible walls, the meniscus slope can be approximated.

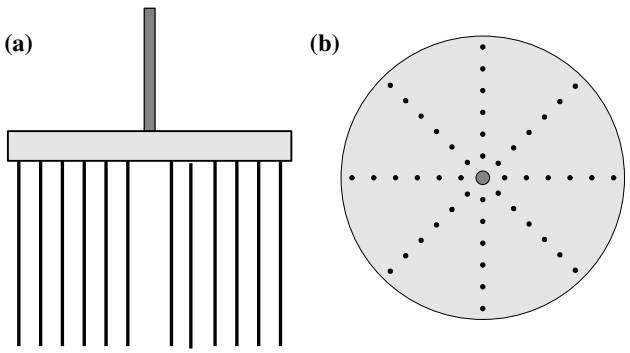

Fig. 4 The schema of the meniscus shape measurement device, **a** front view, **b** bottom view

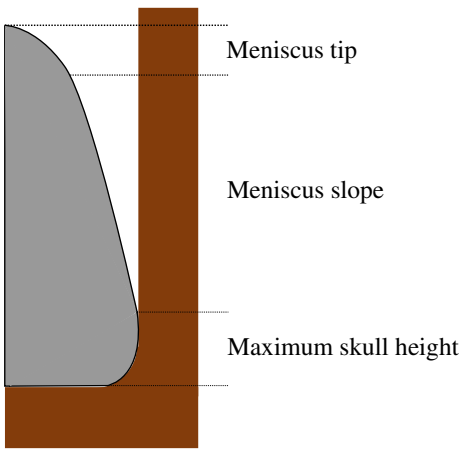

Fig. 5 Maximum skull height and its relation to the meniscus shape

4 Results

4.1 Thermal Measurements

First, the emissivity of the molten metal was assessed. After reaching the steady-state conditions for the considered power input, the immersion thermocouple was placed in the liquid medium. The sinking of the thermocouple was recorded via the IR camera. During the post-processing of the IR images, the emissivity of the recorder surface was adjusted to achieve a temperature similar to that measured with the immersion thermocouple. The temperature field used for that comparison is marked in Fig. 6. Both pictures were captured for Variant A. The thermocouple was sunk into the metal immediately after the steady state conditions were obtained. For the better visualisation of the immersion thermocouple position, the temperature scales for Fig. 6a, b are different. The temperature field presented in Fig. 6 was recorded immediately after the meniscus of the liquid metal formed. Then, the thermocouple was immersed into the metal when the steady-state conditions were achieved. The temperature of the free surface was approximately the same for both images, and the thermocouple was positioned above the metal to heat up the coating up before immersing it into the medium. Then, the emissivity of the spot marked in Fig. 6 (with a circle) was changed until the mean temperature of the spot was similar to the temperature recorded by the thermocouple. That spot consisted of approximately

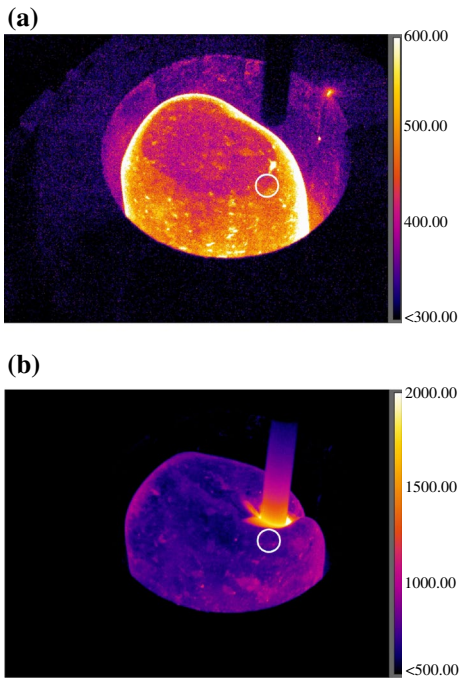

Fig. 6 The temperature field (°C) of the molten metal **a** with the immersion thermocouple outside and **b** inside the molten metal

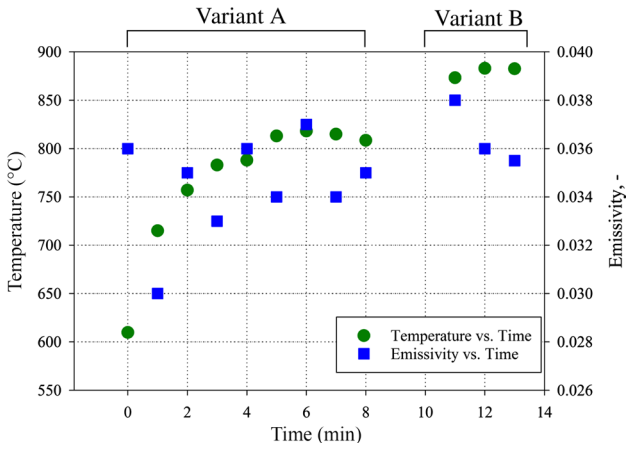

Fig. 7 The temperature and emissivity of the molten metal for Variant A and Variant B

1000 pix of the IR camera sensor. That procedure was repeated within 1-min intervals for 8 min. As a result, the emissivity of the liquid metal for a given power input as a function of time was evaluated. The results of the evaluation of the thermocouple readings are presented in Fig. 7. According to the results presented in Fig. 7, the time average emissivity of the marked spot was 0.034 and 0.037 for Variant A and Variant B, respectively.

Analysing the values presented in Fig. 7, it can be seen that, as expected, the temperature of the alloy increased for the higher power input. The time averaged temperature for the higher power input delivered to the crucible (Variant B) was approximately 13% higher than that for Variant A. Notably, the increase in the generator power by 15% did not significantly affect the temperature of the liquid metal. Consequently, the relatively small temperature increase did not cause the notable emissivity change of the free surface of the metal. That relatively small temperature increase is mostly a result of the intensive cooling of the crucible.

As it can be seen in Fig. 6, the temperature field captured within the IR camera is considerably non-homogeneous, which is an effect of the small amount of oxidation products floating on the metal surface. The emissivity of the visible aluminium oxides is slightly different than the emissivity of the molten medium. Hence, some lower temperature spots can be noticed in Fig. 6. Notably, the oxidation effects were present even for the relatively high vacuum. The non-homogeneous characteristic of the temperature and the emissivity field is primarily related to the refining process of the molten medium and is secondarily related to the oxidation phenomenon.

Regarding the IR measurements, the measurements should be conducted in a way that eliminates the influence of the reflected temperature on the measurement results. Unfortunately, due to the industrial character of the

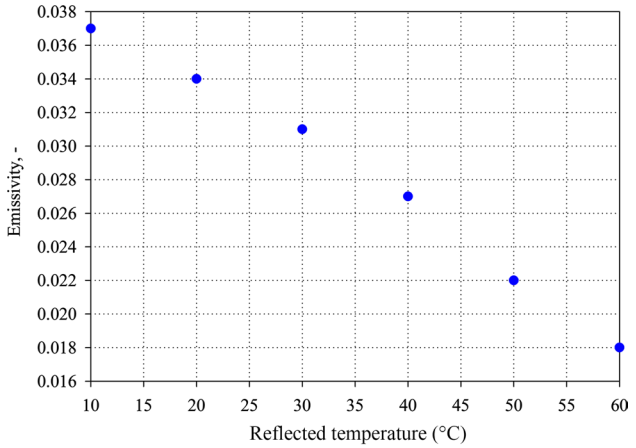

Fig. 8 The assessment of the influence of the area-averaged reflected temperature on the emissivity of molten aluminium

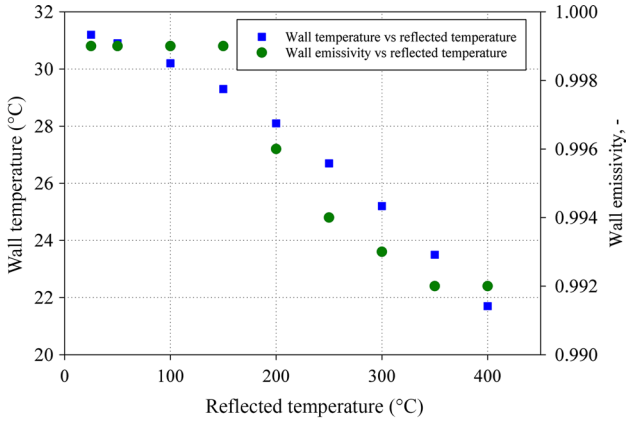

Fig. 9 The influence of the reflected temperature on the IR reading of the graphite covered crucible wall and the wall emissivity

investigated CCF unit, the elimination of the all radiation sources that emit heat on the liquid metal was impossible. The crucible wall inner surface and the furnace chamber inner walls emit some heat on the surface area of the processed medium. Therefore, the influence of that heat emission was evaluated in a similar manner to that in [18]. That is, the crucible wall area and the furnace inner area were assessed, and then the area-weighted average temperature of the reflecting surfaces was assessed. The influence of that parameter on the calculated emissivity is presented in Fig. 8. As shown in Fig. 8, the increase in the reflected temperature results in smaller emissivity values. This trend results from the measurement method implemented by the IR camera. Considering that the IR camera measures the sum of the emitted and reflected energy, the compensation of the reflected heat is accounted for by a decrease of the temperature of the measured object. Consequently, the calculated emissivity must decrease in order for the IR measured surface temperature to match the temperature recorded by the thermocouple. According to the results presented in Fig. 8, the reflected temperature notably affects the computed emissivity. Nevertheless, considering that the reflected temperature is area-weighted and the biggest surface that is emitting heat on the molten metal is the furnace inner wall, the variation in the reflected temperature is very small during the melting process. It should be pointed out that the recorded values of the emissivity showed a good agreement with the literature data for the solid aluminium. On the other hand, the emissivity of the liquid aluminium reported in the literature is usually ten times higher. The reason of that discrepancy may be caused by the temperature measurements procedure. Namely, the temperature reading could be affected by the immersion thermocouple position and the depth of the immersion of the sensor.

To assess the temperature of the crucible, the walls of the device were partially covered with graphite paint. The emissivity of the used paint is very high and is assumed to be 0.99. The temperature of the painted spot was measured using the IR camera. Then, the temperature of the spot covered with graphite and the wall surface next to the spot were assumed to be the same. Consequently, the IR temperature measurements of the spot of the known emissivity were used to evaluate the emissivity of the unpainted crucible wall. The emissivity of the wall as evaluated with this approach was 0.89.

The temperature of the crucible walls is strongly related to the reflected temperature of the molten metal. Considering that the temperature of the molten metal is significantly higher than that of the crucible walls, the influence of the reflected temperature on the emissivity is presented in Fig. 9. As shown in Fig. 9, for a relatively wide variation of the reflected temperature the change of the temperature of the walls recorded with the IR camera was insignificant. Consequently, the reflected temperature values did not affect the evaluated emissivity of the actual crucible walls. According to the presented results, the emissivity of the walls was approximately 0.99 for all considered reflected temperatures. The high emissivity values are the result of the oxidation of the crucible walls and the roughness of the wall surfaces. Additionally, during the refining of the processed metal, some of the oxidation products, e.g., aluminium oxide, stick to the crucible. Consequently, the roughness of the crucible surface increased notably. As a result, the emissivity of the inner crucible walls is approximately 1.

4.2 Skull Shape

As previously mentioned, the skull generation during the process is an important factor from the metal purification point of view. Moreover, as the numerous authors suggest,

Fig. 10 The skull profile for Variant A

Fig. 11 Maximum skull height and its relation to the meniscus shape

the skull which was in direct contact with the cooled crucible bottom was responsible for the most significant heat losses during the melting process [17, 26]. That mechanism prevented the load from the superheating. On the other hand, the skull thickness should be minimised in order to minimise the load losses. Therefore, the skull shape and weight were investigated during the study. The skull thickness and shape were evaluated for Variants A and B, described previously, and additionally for the 70% of the generator load that corresponds to the 4.49 kA current at a frequency of 7.22 kHz. The mass of the skull was investigated for Variant A. For Variant A the melting process was the most stable and guaranteed fully repeatable results. The average skull weight gathered for Variant A was 178 g. Hence, the average loss of the charge was 13%. The amount of the skull was strongly related to the power input during the process. The weight of the skull decreased along with the increase in the power delivered by the coil. For that crucible construction, it was impossible to eliminate skull generation. Nevertheless, a smaller mass of the load or a higher power input could result in a smaller mass of the generated skull.

The shape of the skull was also analysed. That analysis was primarily focused on the skull thickness and height near the walls. To capture the skull thickness and shape, the collected skulls were cut along the diameter. Such a cut is presented in Fig. 10. The characteristic shape of the skull where it contacts the crucible wall is also visible in that figure. The jagged character of the skull sides is a result of the contact of the molten metal with the alternating cooled crucible segments and the slit fillings. Therefore, the tooth-shaped parts of the skull that were close to the cooled part of the crucible segment, i.e., the centre of each segment, are notably higher compared to the parts directly contacting the slits. As it shown in Fig. 10, the jags are notably higher on one side of the skull. This phenomenon is caused by the rotation of the crucible during the metal casting. During the process, a part of the molten metal that was distributed on the crucible side corresponding to the rotation direction was in the direct contact with the crucible walls. The jags visible in Fig. 10 are formed mostly at the centre of the crucible walls segments. That part of the segments is intensively cooled. Consequently, the unmolten metal on the crucible bottom sticks to the centre of the crucible segments and freezes on it. That behaviour of the processed metal is presented in Fig. 11. As shown in Fig. 11, the metal at the crucible bottom is mostly molten, but the parts of the load that are distributed near the crucible segments centre stuck to the crucible wall. Therefore, to eliminate or minimise the loss of the processed metal caused by that mechanism, the cold crucible walls segments should be carefully designed. Moreover, the presented mechanism of the skull jags generation should accounted for when mathematically modelling the melting process in such a crucible. To evaluate the shape of the skull surface shape, the thickness of the skull was measured along the skull diameter, i.e., the thickness was measured every 0.5 mm along the diameter of the skull. Next, the collected points were used to generate the skull surface profile. Such profiles for various power inputs applied immediately before the casting of the metal are presented in Fig. 12. As shown in Fig. 12, the skull shape was affected by the amount of energy delivered to the metal. The skull thickness was evaluated for three variants of the current and the frequency for the three power inputs, namely, 50%, 65% and 70% of the generator power. According to the results presented in Fig. 12, the thickness of the skull decreased with the increasing power input. The skull thickness decreases with the increase in the power input. The average skull thickness for the considered variants were 1.25 cm, 0.74 cm and 0.70 cm for 50%, 65% and 70%, respectively. Comparing the average thickness for the lowest and highest considered power inputs, it is noticeable that the average value of the thickness was reduced by approximately 45%. However, the difference between the

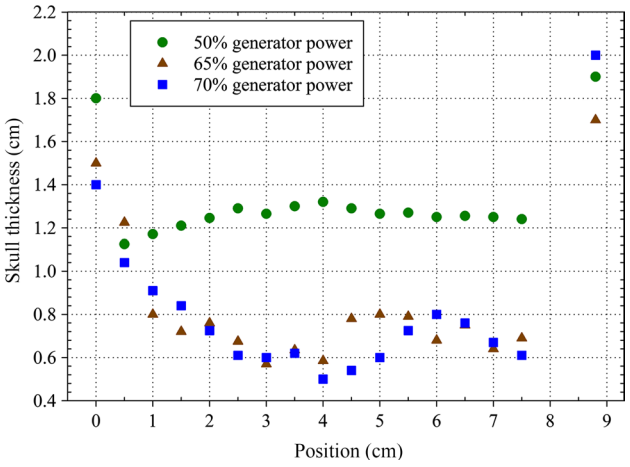

Fig. 12 The skull surface profile for various power inputs

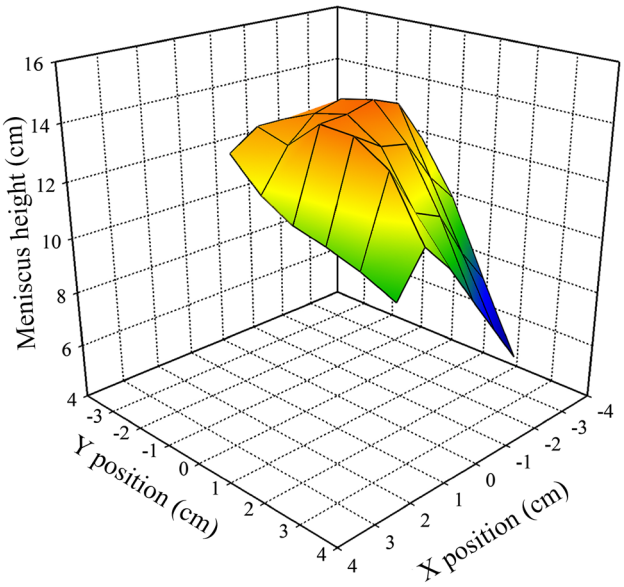

Fig. 13 The meniscus top surface for the 1.3 kg load with 65% of the generator power

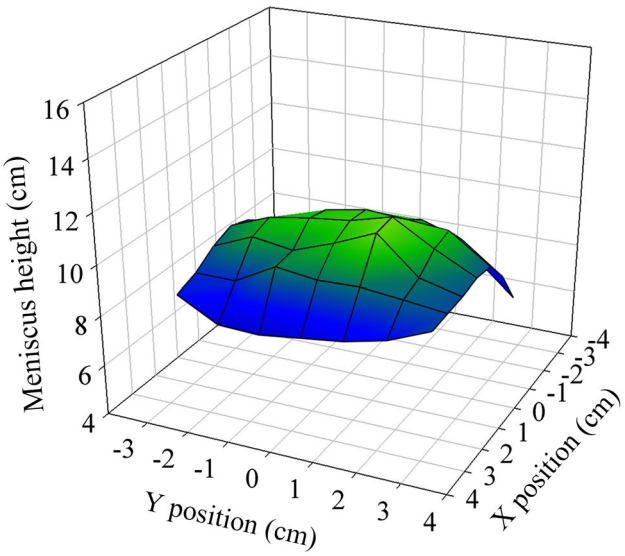

Fig. 14 The meniscus top surface for a 1.3 kg load with 20% of the generator power

skulls gathered for the 65% and 75% generator power can be considered as negligible. The average height of the skull at the crucible walls was 2.5 cm. Unlike to skull thickness, the height of the skull near the crucible walls was approximately the same for all considered cases.

4.3 Shape of the Meniscus

The assessment of the meniscus shape was the most challenging part of this study. The construction of the analysed furnace was unsuitable for any additional measuring equipment to be installed inside the device. Nevertheless, the shape of the meniscus and the free surface area are very important parameters from the CCFs refining process point of view, since the free surface area should be increased to improve the evaporation from the considered metal or alloy surface and consequently improve the refining process of the metal. Moreover, the information about the meniscus shape and its area is significant for model validation. The shape of the meniscus is crucial information for the model fidelity analysis. Therefore, the previously described in-house developed device was used to capture the shape of the tip of the meniscus.

The meniscus shape was assessed during to the melting processes for various initial load shapes and masses, as well as for the various power inputs. Initially, the load was cylinder-shaped for all considered cases. The diameters of the cylinders were 80 mm for all the investigated loads. The initial heights of the loads were 100 mm and 120 mm, which correspond to 1.3 kg and 1.6 kg, respectively. For the 1.3 kg load, the studied power inputs were 20% and 65% of the generator power, while for 1.6 kg load, the power input was 35% of the generator power. The 35% and 65% power inputs guaranteed the meniscus height was equal to the crucible wall height for the 1.3 kg and 1.6 kg loads, respectively. For such power inputs, the mass of the skull decreased. In the case of the higher power inputs, the meniscus is significantly higher than the crucible and the coil. Consequently, the molten metal tends to slip out the crucible. Therefore, the power input should be adjusted for the initial shape and mass of the load.

To visualise the meniscus shape, the surface plots of the meniscus tip are presented in Figs. 13, 14 and 15. In these figures, the shape of the meniscus tip for various cases is presented. As can be seen, the shape of the meniscus tip

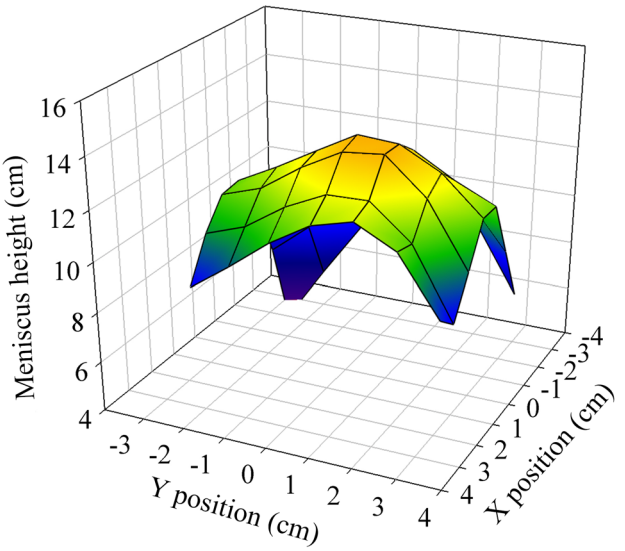

Fig. 15 The meniscus top surface for a 1.6 kg load with 35% of the generator power

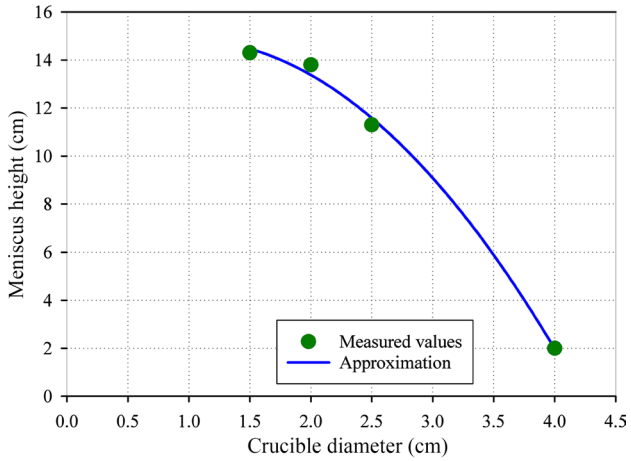

Fig. 16 The slope of the meniscus along the half of the crucible diameter, measured values (green) and approximation (blue) for 1.3 kg load and 65% of generator power. (Color figure online)

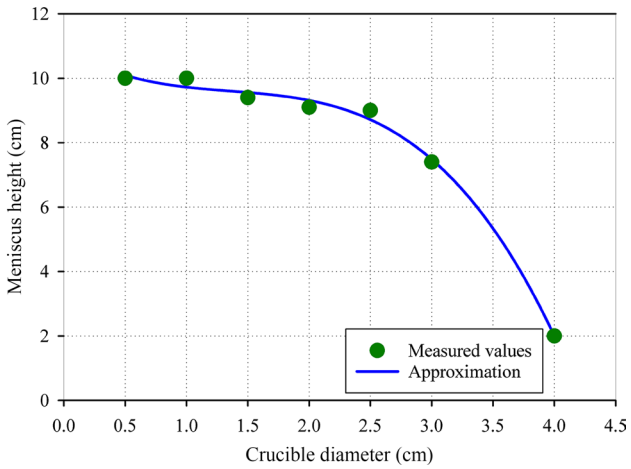

Fig. 17 The slope of the meniscus along half of the crucible diameter, measured values (green) and approximation (blue) for a 1.3 kg load with 20% of the generator power. (Color figure online)

varies with the variation of the load mass or power input. In the case of the 1.3 kg load with a 20% generator power, the meniscus can be seen to be significantly lower than in the case of the higher power inputs. However, it can be seen that the shape of the meniscus tips presented in Figs. 13 and 15 are similar. In both cases, the tip of the meniscus are rather flat. The slope of the meniscus presented in Fig. 13 is significantly steeper compared to those presented in Figs. 14 and 15. As the result of that steep character of the meniscus, less of the processed metal is in the direct contact with the crucible. In such a case, a higher purity of the cast alloy or metal can be achieved. Additionally, the meniscus of the 1.3 kg charge with a 65% power input can be seen to be slightly tilted. The tilt of the meniscus tip that was captured and is presented in Fig. 13 may be the result of the oscillating movement of the meniscus, which was also observed with the high-speed camera during the experiments.

Another parameter that can be used to assess the refining process of the charge is the free surface area. As described in Sect. 3 and illustrated in Fig. 5, it assess the area of the surface, the meniscus tip profile and the height of the skull at the walls were used. It was assumed that the height of the skull that stuck to the crucible wall was 2 cm for all three cases. Then, the points collected during the meniscus tip measurements were used to generate the profiles of the meniscus slope along the crucible bottom diameter. Due to the limited number of collected points during the meniscus tip measurements, the approximation functions were used to calculate the assessments of the slope shape and to calculate the free surface area. The points used for the approximation and the approximated profiles are presented in Figs. 16, 17 and 18.

To generate these profiles, the commercial Systat *SigmaPlot* v. 14 software was used ([27]). The generated approximation functions, the corresponding coefficient of determination (R^2) and the calculated free surface area are listed in Table 2. The R^2 for all the approximation functions were higher than 0.99. As expected, the higher power input in the 1.3 kg load case resulted in an increase of the free surface area. Comparing the results for the similar maximal meniscus heights (Variants A and A.2 in Table 2), the free surface area can be seen to be larger in the case with a lower mass of the charge. Accounting for the initial height of the charge being 20 mm lower for the 1.3 kg case, the free surface area of the meniscus should be lower in that case. However, considering the number of points used to approximate the meniscus slope and tip

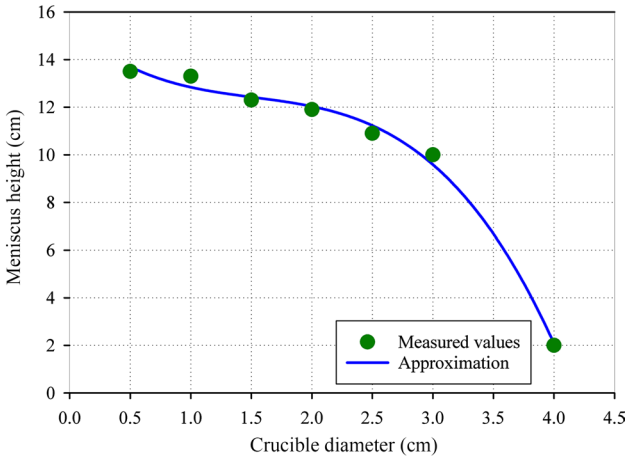

Fig. 18 The slope of the meniscus along half of the crucible diameter, measured values (green) and approximation (blue) for a 1.3 kg load with 35% of the generator power. (Color figure online)

for case 1, the fidelity of the calculated free surface area may be poor. Nevertheless, the obtained results for the free surface area assessment can be used for the general evaluation of the evaporation surface of the molten metal. Notably, the results presented in Table 2 are on the same level as those presented in the literature for vacuum induction furnaces (VIM), e.g. [28]. The meniscus shape and height were mostly affected by the electromagnetic forces inside the load. The detailed numerical analysis of the electromagnetic forces inside the load and its influence on the molten metal behaviour was presented in [29] and [26]. According to the results presented in those papers showed that the turbulence intensity was the highest in the regions where the electromagnetic forces were the strongest. Moreover, the variation of the electromagnetic forces for various power inputs affected the height of the meniscus. The variation of the meniscus height presented in this paper showed similar trends to that presented in [16].

According to the results listed in Table 2,the melting of a greater amount of processed metal or alloy in the investigated CCF is more efficient. The free surface area of the 1.6 kg charge (Variant A.2) was smaller by only 8% as compared to the 1.3 kg charge with 65% of the power input (Variant A). However, the power applied to achieve the free surface area in Variant A.1 was 30% lower than that in Variant A. Hence, to minimise the power consumption during the melting process and simultaneously maximise the free surface area of the meniscus, heavier charges should be considered. The proper selection of the charge size and the power input guarantee a process with effective evaporation of impurities from the processed metal that is power efficient.

5 Conclusions

This manuscript focuses on the experimental analysis of aluminium alloys in cold crucible furnaces. The investigated alloy was composed of 99% aluminium and 1% zinc (mass). The entire studied process was conducted on a small scale but using an industrial-type cold crucible furnace manufactured and delivered by the *Seco-Warwick* company. That device is equipped with a 200 kW generator, a pump system and a process water chiller.

The melting process was conducted for various currents and frequencies and consequently various power inputs. The quasi-steady conditions were obtained for the considered variants. For the temperature measurements, an IR camera and an immersion thermocouple were used. In addition, the molten metal meniscus shape was investigated within the in-house developed device. The last part of the investigation was the analysis of the not molten part of the metal, the so-called skulls, that are typical for that process. The skull thickness and the skull height were analysed during the measurements.

During the temperature measurements, the alloy temperature and emissivity were analysed. The comparison of the IR camera results and the immersion thermocouple showed that the emissivity of the considered alloy was evaluated to be the very low value of 0.03 which was significantly higher than the emissivity of the liquid aluminium presented in literature. Moreover, the emissivity of the crucible walls was evaluated. According to the gathered results, the emissivity of the crucible walls was 0.99. That very high value

Table 2 The free surface area of the meniscus for the investigated power inputs and load sizes

Variant	Case	Approximation function	R^2	Free surface area, m^2
Variant A	1.3 kg load and 65% of generator power	$y = 13.52 + 2.74x - 1.41x^2$	0.997	0.0251
Variant A.1	1.3 kg load and 20% of generator power	$y = 10.94 - 2.36x + 1.52x^2 - 0.37x^3$	0.995	0.0172
Variant A.2	1.6 kg load and 35% of generator power	$y = 15.44 - 4.64x + 2.61x^2 - 0.57x^3$	0.994	0.0231

was mostly caused by the layer of the oxides that cover the crucible walls and increase the roughness of the walls.

The skull weight for the various power inputs and the average skull weight were defined. The average mass of the skulls collected during the measurements campaign was 178 g, which was approximately 13% of the initial mass of the processed alloy. Additionally, the presented results show that the skull thickness is strongly related to the power input applied before the metal casting. In general, a higher power input reduced the skull weight. The skull surface profile analysis showed that the skull thickness is more or less constant along the skull diameter.

Finally, the device that was developed in-house was used to capture the shape of the meniscus tip surface. During that analysis, the points describing the shape of the meniscus tip were gathered. Next, these points were used to create the surface plots of the meniscus tip and to calculate the free surface area of the meniscus. The results recorded for that investigation show that the process was more energy efficient in the cases with higher amounts of the processed metal.

The proposed methodology of the experimental investigation can be useful for analysis of different metals and alloys in CCFs. Due to the industrial characteristics of the investigated melter, a higher accuracy of the measurements, especially in terms of the meniscus shape measurements, is difficult to achieve. Nevertheless, further research will be focused on improving the measurement instruments, and an analysis of titanium-based alloys will be conducted to improve the casting of that metal.

Acknowledgements Financial assistance was provided by grant no. 2014/13/B/ST8/02364 funded by the National Science Centre, Poland and is here acknowledged. The work of MP was also partially supported by the Rector's research grant provided by SUT (08/060/RGJ17/0108), and the work of JS was partially supported by the statutory research fund of the Faculty of Power and Environmental Engineering, Silesian University of Technology, Gliwice, Poland.

References

1. A. Morita, H. Fukui, H. Tadano, S. Hayashi, J. Hasegawa, M. Niinomi, Mater. Sci. Eng. A **280**(1), 208 (2000)
2. A.V. Fadeev, V.E. Bazhenov, A.V. Koltygin, Russ. J. Non-Ferr. Metals **56**(1), 26 (2015)
3. M.I. Ojovan, *Handbook of Advanced Radioactive Waste Conditioning Technologies* (Woodhead Publishing, Sawston, 2011)
4. A. Choudhury, M. Blum, Vacuum, in *Proceedings of the 13th International Vacuum Congress and the 9th International Conference on Solid Surfaces*, vol 47(6) (1996), p. 829
5. J. Song, B. Min, J. Kim, H. Kim, S. Hong, S. Chung, Int. Commun. Heat Mass Transf. **32**(10), 1325 (2005)
6. G. Sugilal, Int. J. Therm. Sci. **47**(7), 918 (2008)
7. S. Spitans, E. Baake, A. Jakovics, H. Franz, Magnetohydrodynamics **51**(3), 567 (2015)
8. A. Smalcerz, B. Oleksiak, G. Siwiec, Arch. Metall. Mater. **60**(3A), 1711 (2015)
9. M. Dumont, R. Ernst, C. Garnier, G. Hasan, P. Petitpas, in *International Conference on Electromagnetic processing of materials EPM*, Beijing (2012)
10. R. Chen, Y. Yang, Q. Wang, H. Ding, Y. Su, J. Guo, J. Mater. Process. Technol. **255**, 242 (2018)
11. J. Yang, R. Chen, H. Ding, J. Guo, Y. Su, H. Fu, J. Mater. Process. Technol. **213**(8), 1355 (2013)
12. M. Kaneda, T. Tagawa, H. Ozoe, Exp. Thermal Fluid Sci. **30**(3), 243 (2006)
13. Z. Li, J. Li, X. Li, M.J. Ni, Exp. Thermal Fluid Sci. **82**, 240 (2017)
14. S.T. Johansen, Exp. Thermal Fluid Sci. **26**(6), 739 (2002)
15. P. Bulinski, J. Smolka, S. Golak, R. Przylucki, L. Blacha, R. Bialecki, M. Palacz, G. Siwiec, Arch. Metall. Mater. **60**(3A), 1575 (2015)
16. V. Bojarevics, K. Pericleous, R.A. Harding, M. Wickins, Metall. Mater. Trans. B **35**(4), 785 (2004)
17. K. Pericleous, V. Bojarevics, G. Djambazov, R. Harding, M. Wickins, Applied Mathematical Modelling, in *Selected papers from the Third International Conference on CFD in the Minerals and Process Industries*, vol. 30(11) (2006), 1262
18. P. Bulinski, J. Smolka, S. Golak, R. Przylucki, M. Palacz, G. Siwiec, J. Lipart, R. Bialecki, L. Blacha, Appl. Therm. Eng. **124**, 1003 (2017)
19. P. Bulinski, J. Smolka, S. Golak, R. Przylucki, M. Palacz, G. Siwiec, B. Melka, L. Blacha, Int. J. Heat Mass Transf. **126**, 980 (2018)
20. P. Bulinski, J. Smolka, G. Siwiec, L. Blacha, S. Golak, R. Przylucki, M. Palacz, B. Melka, Appl. Therm. Eng. **150**, 348 (2019)
21. M.C. Song, Y.H. Moon, Appl. Therm. Eng. **98**, 98 (2016)
22. S. Matsuzawa, G. Yoshikawa, K. Hirata, F. Miyasaka, Y. Nakai, M. Tsuda, Y. Komemushi, I.E.E.E. Trans, IEEE Trans. Magn. **51**(3), 1–4 (2015)
23. R. Chen, Y. Yang, X. Gong, J. Guo, Y. Su, H. Ding, H. Fu, Metall. Mater. Trans. B **48**(6), 3345 (2017)
24. A. Naranjo, M.D.P. Noriega, T.A. Osswald, A. Roldan-Alzate, J.D. Sierra, *Plastics Testing and Characterization—Industrial Applications* (Hanser Publishers, Munich, 2008)
25. D. Hewak, Properties, Processing and Applications of Glass and Rare Earth-Doped Glasses for Optical Fibres (Institution of Engineering and Technology, 1998)
26. V. Bojarevics, K. Pericleous, R. Brooks, Metall. Mater. Trans. B **40**(3), 328 (2009)
27. Systat, Systat Sigmaplot User's Manual (2017)
28. G. Siwiec, P. Bulinski, M. Palacz, J. Smolka, L. Blacha, Arch. Metall. Mater. **62**, 2449 (2018)
29. V. Bojarevics, K. Pericleous, in *IOP Conference Series: Materials Science and Engineering*, vol. 424, 012029